Electronic Supplementary Material (ESI) for Journal of Materials Chemistry A.

Electronic Supplementary Information (ESI)

Contorted Polycyclic Aromatic Hydrocarbon: Promising Li Insertion Organic Anode

Jaehyun Park,‡[a] Cheol Woo Lee,‡[bc] Se Hun Joo,‡[a] Ju Hyun Park,[a] Chihyun Hwang,[a] Hyun-Kon Song,[a] Young Seok Park,[d] Sang Kyu Kwak,*[a] Seokhoon Ahn*[b] and Seok Ju Kang*[a]

[a]School of Energy and Chemical Engineering, Ulsan National Institute of Science and Technology (UNIST), Ulsan 44919, Korea

[b]Institute of Advanced Composite Materials, Korea Institute of Science and Technology, Jeonbuk 55324, Korea

[c]Applied Materials Institute for BIN Convergence, Department of BIN Convergence Technology and Department of Polymer-Nano Science and Technology, Chonbuk National University, Jeonbuk 54896, Korea

[d]Department of Chemistry, Ulsan National Institute of Science and Technology (UNIST), Ulsan 44919, Korea

*E-mail: skkwak@unist.ac.kr, ahn75@kist.re.kr, sjkang@unist.ac.kr

Keywords: contorted hexabenzocoronene, Li-ion battery, anode, Li insertion, differential capacity

1. Computational Details:

Crystal Structure Prediction. A detailed crystallographic and theoretical polymorphism study of contorted-hexabenzocoronene (c-HBC) was undertaken using the Polymorph module of Materials Studio 2017 R2.[1] The molecular structure of c-HBC, optimized by the density functional theory (DFT) calculation, was used as the starting geometry for the polymorph prediction. The crystal structure prediction was performed sequentially in six steps (i.e., packing, clustering, geometry optimization, clustering, geometry optimization, and clustering) and the entire procedure was repeated three times. In the packing step, Monte Carlo simulated annealing was performed for sampling of the crystal structures within a specific space group. The crystal structure prediction procedures were performed for 10 space groups including $P2_1/c$, $P\bar{1}$, $P2_12_12_1$, $C2/c$, $P2_1$, $Pbca$, $Pna2_1$, Cc, $Pbcn$, and $C2$. In order to achieve sufficiently wide sampling, we set the maximum temperature to 1.5×10^5 K, minimum temperature to 300 K, maximum number of steps to 500,000, number of steps to accept before cooling to 100, minimum move factor to 1.0×10^{-50}, and heating factor to 0.025. In the geometry optimization step, the lattice parameters and atomic positions were relaxed under crystallographic symmetry. In the first geometry optimization step, the c-HBC molecules were treated as rigid bodies. The maximum number of steps was set to 10,000 and the convergence criteria were set to 2.0×10^{-5} kcal mol^{-1} for energy, 0.001 kcal mol^{-1} Å^{-1} for force, 0.001 GPa for stress, and 1.0×10^{-5} Å for displacement. In the clustering step, the clusters of many similar structures were determined, and the lowest energy structure representing each cluster was filtered. The criterion of crystal similarity measure was set to 0.11, which was calculated based on a comparison of radial distribution functions with a cutoff distance of 7 Å and 140 bins. After the final clustering step, the space group symmetry of the predicted crystal structures was reanalyzed. The interatomic interactions for the energy calculation and the geometry optimization were described by COMPASS II force field.[2]

Short-range van der Waals interaction was calculated between pairs of atoms within a cutoff distance of 18.5 Å. Long-range electrostatic interaction was calculated using the Ewald summation method.[3,4]

Monte Carlo (MC) Simulation. To explore the Li-ion insertion sites of c-HBC, Monte Carlo (MC) simulations were performed using the Sorption module of Material Studio 2017 R2.[1] Based on the metropolis algorithm, the GCMC simulations were performed independently 10 times with 100,000 maximum loading steps, 100,000 production steps, and 4 annealing cycles. The interatomic interactions were described by COMPASS II force field with Mulliken charges obtained by DFT calculations.[2,5]

Density Functional Theory Calculation. DFT calculations were performed using the Cambridge Serial Total Energy Package (CASTEP) in Materials Studio 2017 R2.[1,6] The generalized gradient approximation with the Perdew–Burke–Ernzerhof (GGA-PBE) functional was used to describe the exchange correlation potential of the electrons.[7] The interactions between ions and electrons were described by on-the-fly generated ultrasoft pseudopotentials. The plane-wave basis set with a cutoff energy of 600 eV was employed to expand the wave functions. The van der Waals interactions were corrected by Grimme's method.[8] The convergence criterion for self-consistent field calculation was set to 5.0×10^{-7} eV atom^{-1}. Lattice parameters and atomic positions were fully relaxed. The convergence criteria for geometry optimization were set to 5.0×10^{-6} eV atom^{-1} for energy, 0.01 eV Å^{-1} for force, 0.02 GPa for stress, and 5.0×10^{-4} Å for displacement. The Brillouin zone was integrated using a $1 \times 1 \times 1$ k-point grid with the Monkhorst–Pack scheme for all calculations.[9] The formation energy (E_f) of the Li-ion inserted structure as a function of Li-ion content was calculated as follows:

$$E_\mathrm{f} = E_{\mathrm{Li}_n\text{-c-HBC}} - E_\text{c-HBC} - nE_\mathrm{Li}$$

where $E_{\mathrm{Li}_n\text{-c-HBC}}$ is the total energy of the c-HBC crystal with inserted Li-ions, n is the number of inserted Li-ions, $E_{\text{c-HBC}}$ is the total energy of the $\mathrm{R}\bar{3}$ crystal phase of c-HBC, and E_{Li} is the total energy per atom of bcc bulk Li. The voltage profile as a function of Li-ion content was calculated as follows:

$$V(n) = -\frac{E_{\mathrm{Li}_{n_2}\text{-c-HBC}} - E_{\mathrm{Li}_{n_1}\text{-c-HBC}} - (n_2 - n_1)E_{\mathrm{Li}}}{q(n_2 - n_1)}.$$

where $E_{\mathrm{Li}_{n_1}\text{-c-HBC}}$ and $E_{\mathrm{Li}_{n_2}\text{-c-HBC}}$ represent the total energy of the c-HBC crystal with inserted Li-ions, n_1 and n_2 are the numbers of inserted Li-ions ($n_2 > n_1$), E_{Li} is the total energy per atom of bcc bulk Li, and q is the net charge of Li-ions ($q = +1e$). The formation energies (E_f) and voltage profile (V) were calculated without dispersion correction.

2. Polymorph II Crystal Structure

The powder XRD and GIXD patterns of polymorph II showed enhanced reflections at q = 1.04 Å^{-1} and q = 1.15 Å^{-1} and a decreased peak at q = 0.95 Å^{-1}, compared with polymorph II′ (i.e., the $\mathrm{R}\bar{3}$ crystal phase). Except for the differences in the relative intensities of the three peaks, the powder XRD and GIXD patterns between the polymorph II and $\mathrm{R}\bar{3}$ crystal phases were remarkably similar. Therefore, we considered that polymorph II also belongs to the trigonal crystal system but with larger lattice parameters and different intermolecular packing.

The polymorph II crystal structure was solved using the Reflex module of Materials Studio 2017 R2.[1] The parallel tempering algorithm was used with the close contact penalty. As shown in Fig.S9a, the $\mathrm{P3_1}$ and $\mathrm{P3_2}$ crystal phases exhibit the greatest similarities in the XRD patterns, with enhanced reflections at q = 1.04 Å^{-1} while retaining the remaining major peaks. The crystal structures of $\mathrm{P3_1}$ and $\mathrm{P3_2}$ are similar to $\mathrm{R}\bar{3}$ in that three c-HBC molecules are stacked in a hexagonal lattice according to the ABC sequence and oriented in the same direction (Fig. S9b). The only difference is that the c-HBC molecules of the $P3_1$ and $P3_2$ crystal phases are slightly shifted and rotated, which makes the crystal structures metastable and transformed into the $R\bar{3}$ crystal phase after geometry optimization. Even though we confirmed that the different intermolecular stacking enhanced the reflection at $q = 1.04$ Å^{-1}, the crystal structure, which could accurately represent polymorph II, was not identified among the crystal structures solved by the experimental powder XRD pattern and those obtained by polymorph prediction.

In light of the above, we considered the residual Pd impurities, which can be originated from the Pd-catalyzation reactions. Solving the experimental XRD patterns with additional Pd atoms clearly disclosed that the experimental XRD pattern of the polymorph II phase of c-HBC (Fig. S9c and S9e, black line) matched exactly the XRD pattern of $P3_1$ and $P3_2$ with inserted Pd atoms (Fig. S9c and S9e, blue line). The Rietveld refinement result (Fig. S9c and S9e, red line) was found in good agreement with the experimental XRD pattern (Fig. S9c and S9e, black line), as reflected by the negligible differences (Fig. S9c and S9e, green line) and the low final residual factors ($R_p = 3.17\%$ and $R_{wp} = 4.57\%$ for $P3_1$, and $R_p = 3.35\%$ and $R_{wp} = 4.73\%$ for $P3_2$). The results showed that the polymorph II crystal structure does not represent pure c-HBC but rather c-HBC with Pd impurities, as shown in Fig. S9d and S9f.

3. Supporting Information Figures

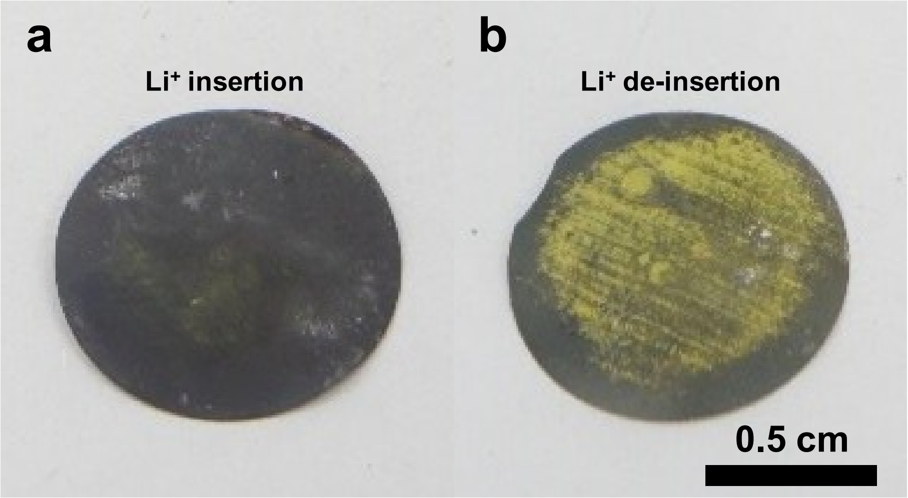

Fig. S1 Digital photographs of the c-HBC anode. (a) after lithium insertion and (b) after de-insertion. The visible black coloration after lithium insertion suggests a lowered band gap of c-HBC. Furthermore, the yellow coloration after lithium desertion indicates the band gap returned to its initial state.

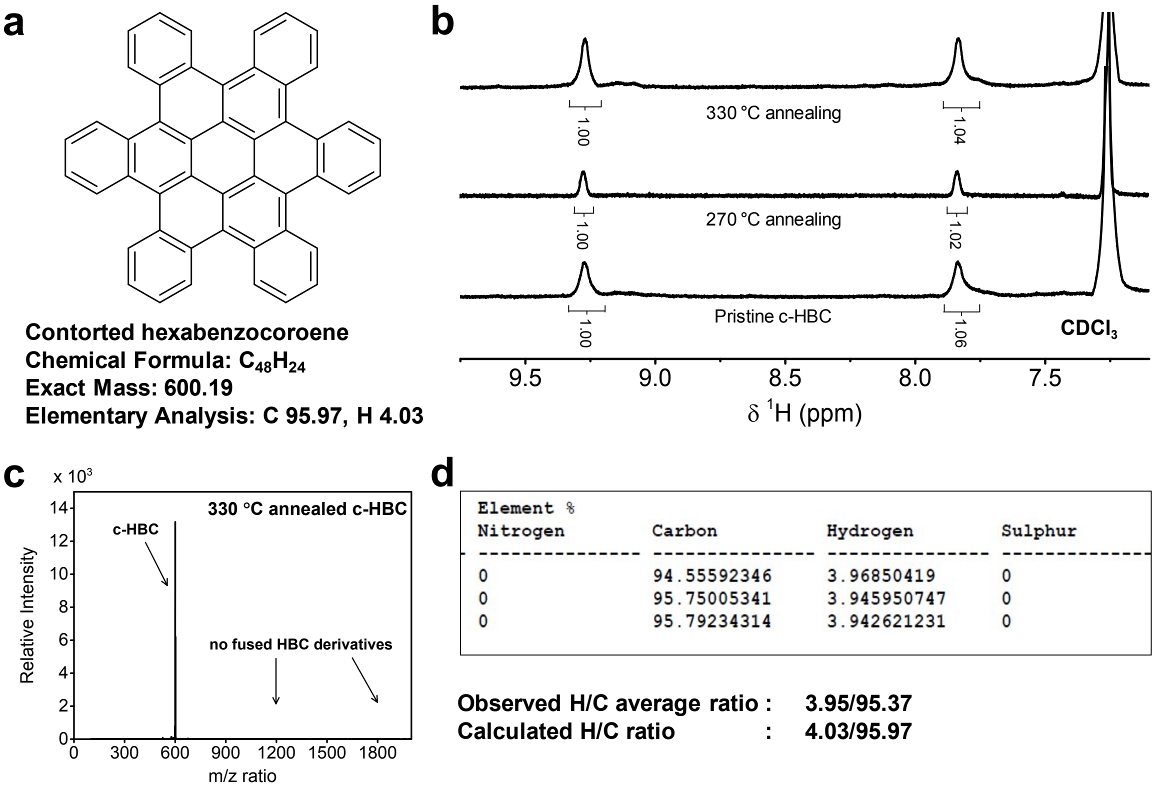

```
Element %
Nitrogen          Carbon            Hydrogen          Sulphur
---------------   ---------------   ---------------   ---------------
0                 94.55592346       3.96850419        0
0                 95.75005341       3.945950747       0
0                 95.79234314       3.942621231       0
```

Observed H/C average ratio : 3.95/95.37

Calculated H/C ratio : 4.03/95.97

Fig. S2 (a) Chemical structure information of c-HBC. (b) ^{1}H-NMR spectra after thermal treatment. (c) Mass spectrum of c-HBC after annealing at 330 °C from laser desorption/ionization time-of-flight (TOF) mass. (d) Elemental analysis of c-HBC after annealing at 330 °C.

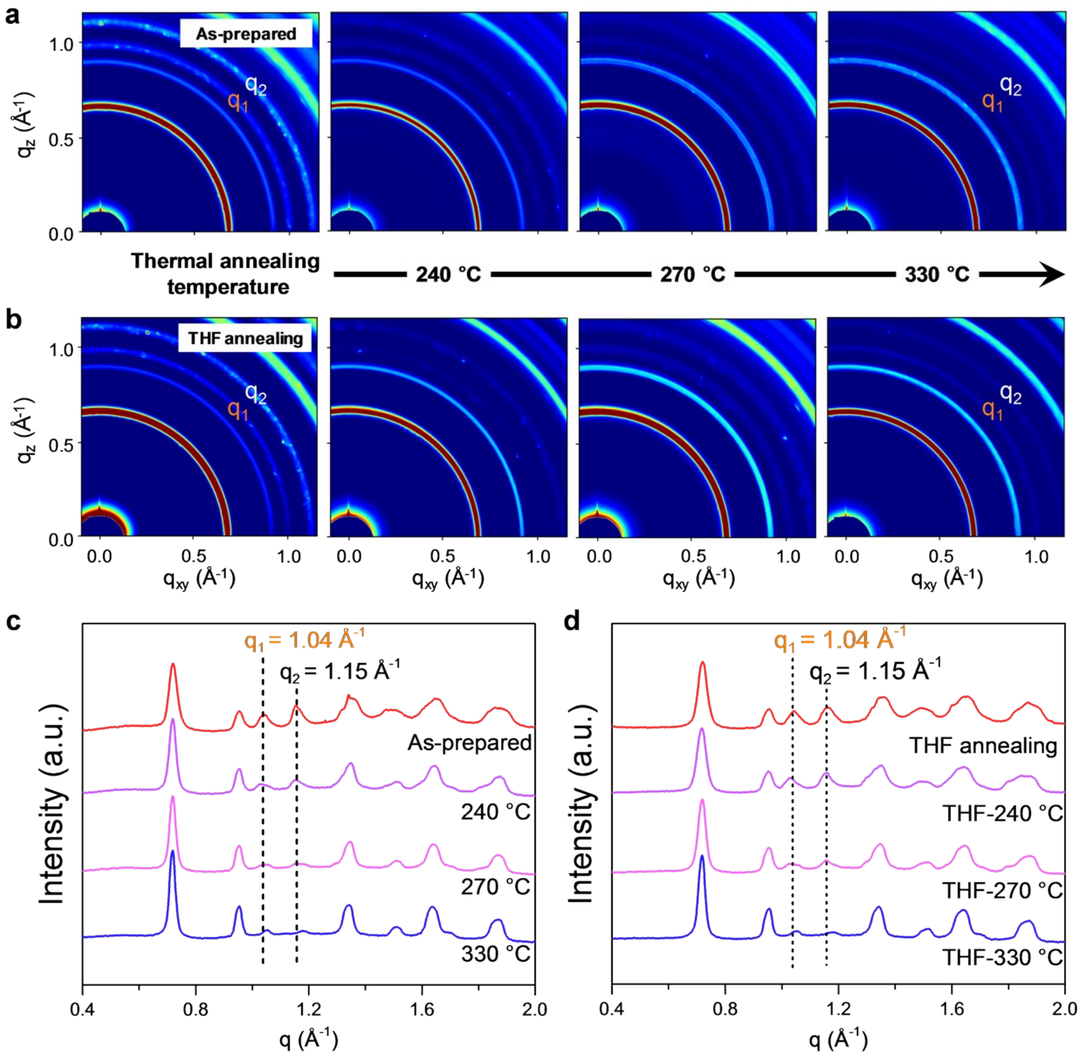

Fig. S3 In situ 2D-GIXD images of (a) as-prepared and (b) THF-annealed c-HBC films on Si wafers as a function of thermal annealing temperature. The diffraction traces of (c) as-prepared and (d) THF annealed c-HBC films reveal significantly enhanced reflection at q = 0.95 Å^{-1} and decreased peaks at q = 1.04 Å^{-1} and q = 1.15 Å^{-1}.

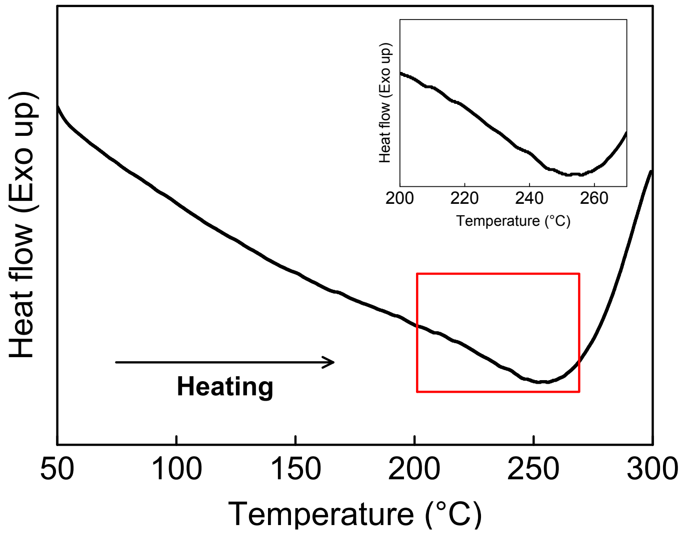

Fig. S4 Differential calorimetry scan of c-HBC powder. The broad endothermic peak was observed near 260 °C (heating ratio: 5 °C min^{-1}).

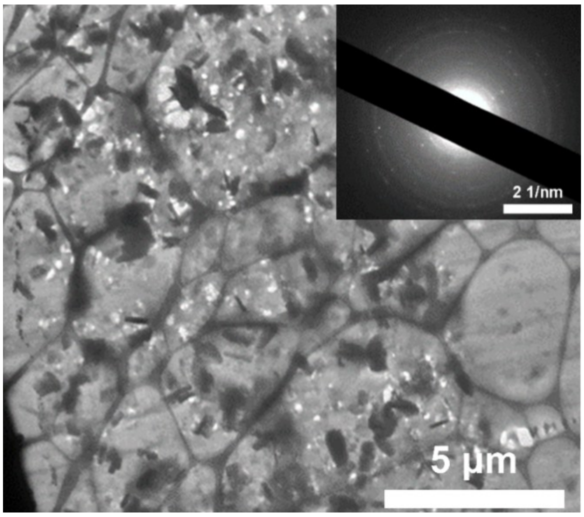

Fig. S5 Low-magnification cross-sectional TEM image of THF-annealed c-HBC film. Inset shows electron diffraction pattern of the selected area of THF-annealed c-HBC film.

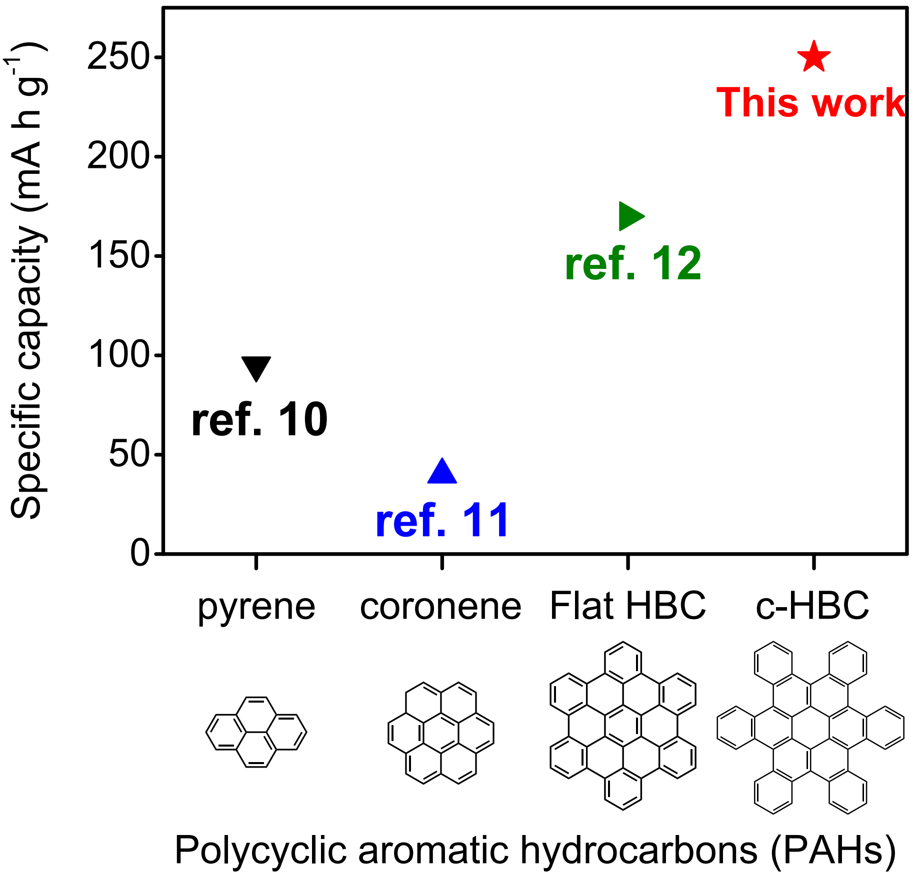

Fig. S6 Plot of specific capacity vs. polycyclic aromatic hydrocarbons (PAHs).

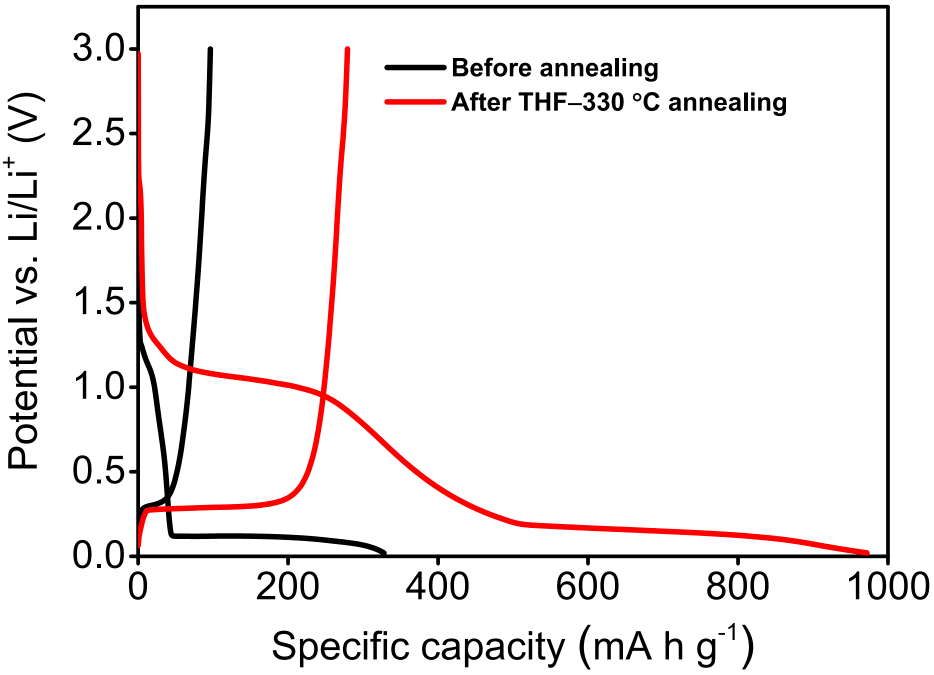

Fig. S7 First galvanostatic discharge-charge voltage profile of c-HBC without (black line) and with annealing treatment (red line)

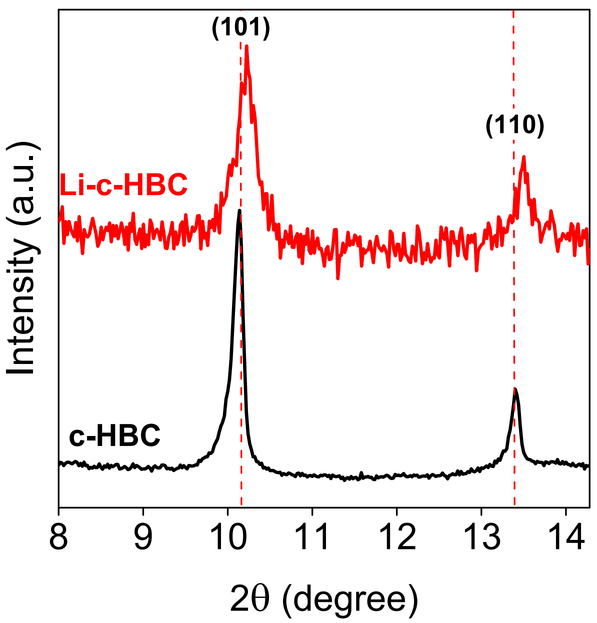

Fig. S8 XRD patterns of pristine (black line) and galvanostatic discharged c-HBC (red line).

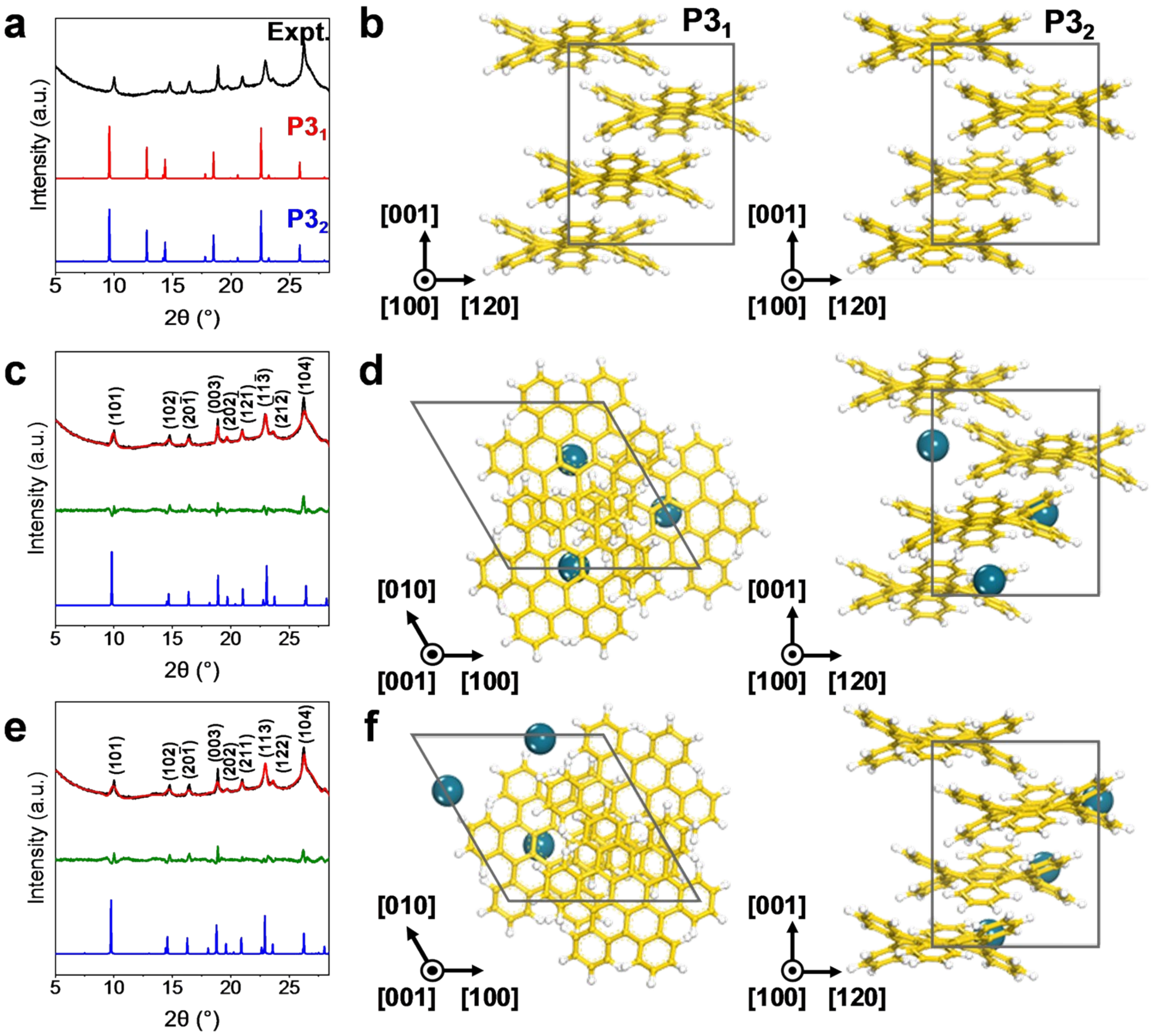

Fig. S9 (a) XRD patterns of polymorph II, P3$_1$, and P3$_2$ crystal phases. (b) Projection views of P3$_1$ and P3$_2$ crystal phases along [100] directions. (c,e) XRD patterns of polymorph II: experimental (black line), Rietveld refined (red line), their difference (green line), and P3$_1$ and P3$_2$ crystal phases with Pd atoms (blue line). (d,f) Projection views of P3$_1$ and P3$_2$ crystal phases with Pd atoms along [001] and [100] directions. Carbon, hydrogen, and palladium are colored yellow, white, and dark cyan, respectively.

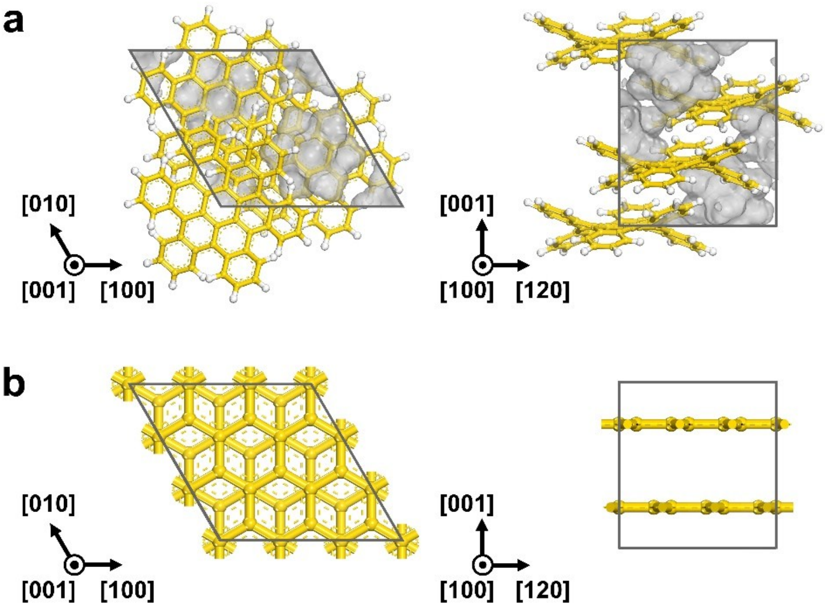

Fig. S10 Projection views of (a) $R\bar{3}$ crystal phase and (b) graphite with Connolly surface along [001] and [100] directions. Carbon and hydrogen are colored yellow and white, respectively.

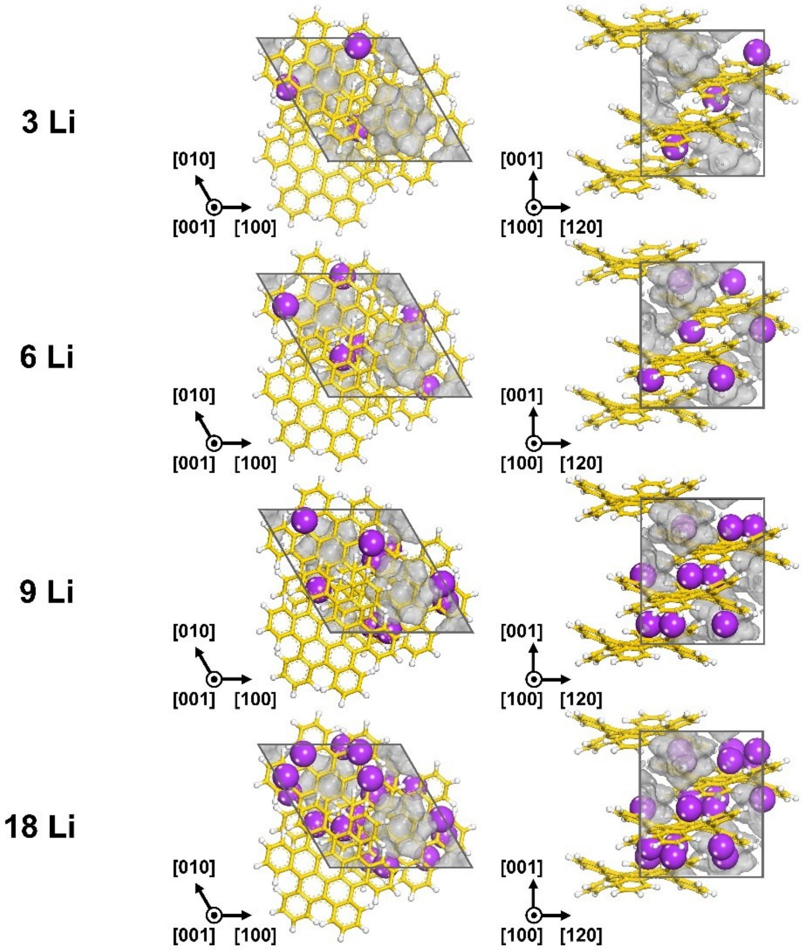

Fig. S11 Projection views of the optimized stable structures of 3, 6, 9, and 18 Li-inserted $R\bar{3}$ crystal phase. Carbon, hydrogen, and lithium are colored yellow, white, and purple, respectively.

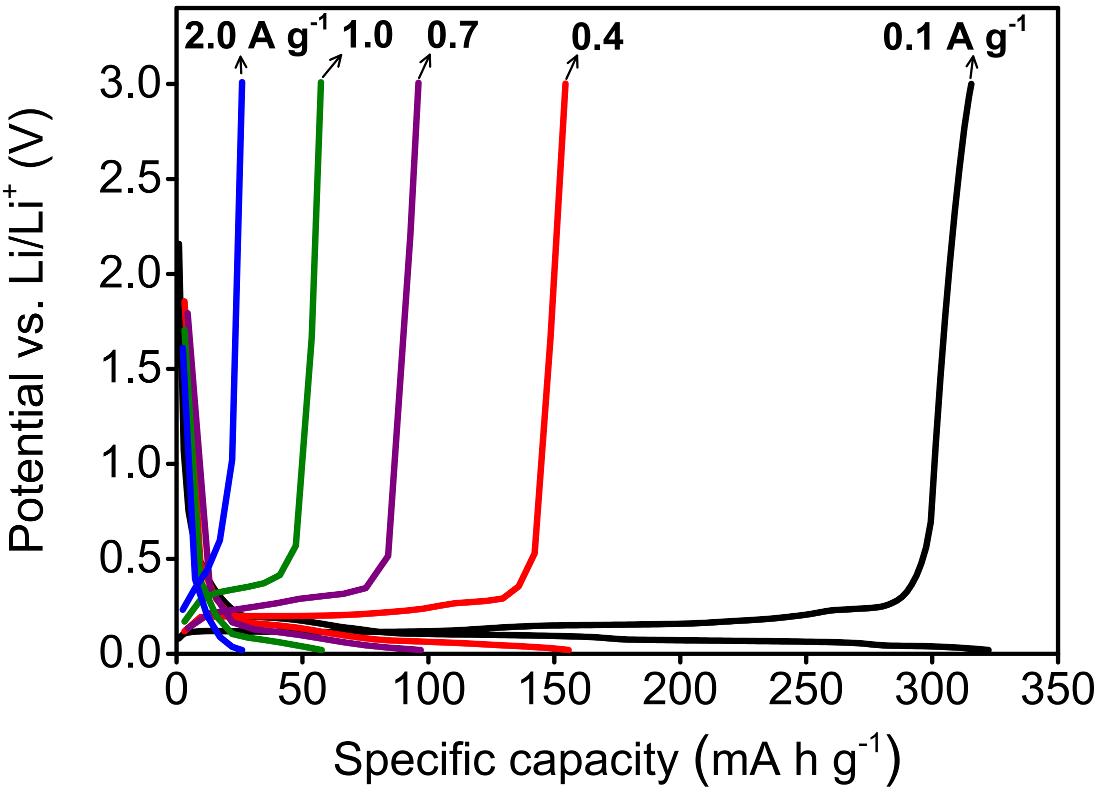

Fig. S12 Galvanostatic discharge-charge voltage profile of graphite anode at various current densities ranging from 0.1 to 2.0 A g^{-1}.

References

1 Materials Studio 2017R2; BIOVIA Inc.: San Diego, CA, 2017.

2 H. Sun, Z. Jin, C. Yang, R. L. Akkermans, S. H. Robertson, N. A. Spenley, S. Miller, and S. M. Todd, *J. Mol. Model*, 2016, **22**, 47.

3 P. P. Ewald, *Annalen der Physik*, 1921, **369**, 253–287.

4 M. P. Tosi, in *Solid State Physics*, eds. F. Seitz and D. Turnbull, Academic Press, 1964, **16**, pp. 1–120.

5 R. S. Mulliken, *J. Chem. Phys.*, 1955, **23**, 1833–1840.

6 S. J. Clark, M. D. Segall, C. J. Pickard, P. J. Hasnip, M. J. Probert, K. Refson, and M. C. Payne, *Zeitschrift für Kristallographie*, 2005, **220**, 567–570.

7 J. P. Perdew, K. Burke, and M. Ernzerhof, *Phys. Rev. Lett.*, 1996, **77**, 3865–3868.

8 S. Grimme, *J. Comput. Chem.*, 2006, **27**, 1787–1799.

9 H. J. Monkhorst and J. D. Pack, *Phys. Rev. B*, 1976, **13**, 5188–5192.

10 J. C. Bachman, R. Kavian, D. J. Graham, D. Y. Kim, S. Noda, D. G. Nocera, Y. Shao-Horn and S. W. Lee, *Nat. Commun.*, 2015, **6**, 7040

11 I. A. Rodriguez-Perez, Z. Jian, P. K. Waldenmaier, J. W. Palmisano, R. S. Chandrabose, X. Wang, M. M. Lerner, R. G. Carter and X. Ji, *ACS Energy Lett.*, 2016, **1**, 719–723

12 K. Mukai, M. Harada, Y. Kikuzawa, T. Mori and J. Sugiyama, *Electrochem. Solid-State Lett.,* 2011, **14**, A52–A55